



Hubble WFC3 Spectroscopy of the Habitable-zone Super-Earth LHS 1140 b

Billy Edwards^{1,3}, Quentin Changeat^{1,3}, Mayuko Mori², Lara O. Anisman¹, Mario Morvan¹, Kai Hou Yip¹,
Angelos Tsiaras¹, Ahmed Al-Refaie¹, Ingo Waldmann¹, and Giovanna Tinetti¹

¹Department of Physics and Astronomy, University College London, London, UK; billy.edwards.16@ucl.ac.uk

²Department of Astronomy, University of Tokyo, Tokyo, Japan

Received 2020 September 8; revised 2020 October 25; accepted 2020 October 30; published 2020 December 23

Abstract

Atmospheric characterization of temperate, rocky planets is the holy grail of exoplanet studies. These worlds are at the limits of our capabilities with current instrumentation in transmission spectroscopy and challenge our state-of-the-art statistical techniques. Here we present the transmission spectrum of the temperate super-Earth LHS 1140b using the Hubble Space Telescope (HST). The Wide Field Camera 3 (WFC3) G141 grism data of this habitable-zone ($T_{\text{eq}} = 235$ K) super-Earth ($R = 1.7 R_{\oplus}$) shows tentative evidence of water. However, the signal-to-noise ratio, and thus the significance of the detection, is low and stellar contamination models can cause modulation over the spectral band probed. We attempt to correct for contamination using these models and find that, while many still lead to evidence for water, some could provide reasonable fits to the data without the need for molecular absorption although most of these cause features in the visible ground-based data which are nonphysical. Future observations with the James Webb Space Telescope would be capable of confirming, or refuting, this atmospheric detection.

Unified Astronomy Thesaurus concepts: [Exoplanet atmospheres \(487\)](#); [Hubble Space Telescope \(761\)](#); [Space observatories \(1543\)](#); [Exoplanet atmospheric composition \(2021\)](#); [Habitable planets \(695\)](#); [Habitable zone \(696\)](#)

1. Introduction

Despite our strong observational bias for detecting large, gaseous giants—similar to Saturn and Jupiter—current statistics from over 4000 confirmed planets show a very different picture: planets roughly between 1 and $10 M_{\oplus}$ are the most abundant planets around other stars, especially around late-type stars (e.g., Dressing & Charbonneau 2013; Howard & Fulton 2016; Dressing et al. 2017; Fulton & Petigura 2018).

Recent population statistics, backed up by theoretical models, reveal a surprising dichotomy in the occurrence rates of small planets. Precise radius measurements from the California-Kepler Survey (CKS), have indicated that they may come in two size regimes: super-Earths with $R_p \leq 1.5 R_{\oplus}$ and sub-Neptunes with $R_p = 2.0\text{--}3.0 R_{\oplus}$, with few planets in between (Fulton et al. 2017; Owen & Wu 2017; Fulton & Petigura 2018). This natural division suggests that for planets larger than $1.8 R_{\oplus}$, volatiles must contribute significantly to the planetary composition (Rogers & Seager 2010; Demory et al. 2011; Nettelmann et al. 2011; Valencia et al. 2013), while smaller ones favor models with more negligible atmospheres (Dressing et al. 2015; Gettel et al. 2016). However, while various evolutionary models have postulated that this dichotomy is due to atmospheric loss, others have questioned it (e.g., Zeng et al. 2019) and only through atmospheric characterization can this hypothesis be thoroughly tested.

The search for rocky planets with signs of habitability and biosignatures form the holy grail of exoplanet atmospheric characterization. Due to their larger relative size when compared to the host star, small planets around M dwarfs have become the focus of this search. The TRAPPIST-1 system of seven Earth-sized worlds (Gillon et al. 2017) provides some of the most intriguing targets for atmospheric characterization. However, due to their lack of prominent features, Hubble Space

Telescope (HST) observations of the four worlds which potentially lie within the habitable zone of the star have ruled out the possibility of a clear, hydrogen-dominated atmosphere (de Wit et al. 2016, 2018).

Thus far the smallest habitable-zone world with a confirmed water vapor detection is the $2.28 R_{\oplus}$, $7.96 M_{\oplus}$ planet K2-18 b (Benneke et al. 2019; Tsiaras et al. 2019). This detection has sparked intense debate regarding the nature of this world: water world or sub-Neptune? Seemingly sitting in the sub-Neptune region of the radius valley, the internal structure of K2-18b remains unknown. Large uncertainties on the radius of the star have caused the planet radius to be poorly defined, also affecting the calculated density. Hence, while the atmosphere of K2-18 b could contain a large amount of hydrogen and/or helium, it could also be a water world (Zeng et al. 2019). With current facilities, the search for atmospheric features of rocky, habitable-zone planets has not been successful thus far.

Here we present the analysis of HST Wide Field Camera 3 (WFC3) G141 observations of a temperate super-Earth. With a radius of $1.7 R_{\oplus}$ and a density of 7.5 g cm^{-3} , LHS 1140b is likely to be a rocky world (Ment et al. 2019) and, with an equilibrium temperature of ~ 235 K, is within the conservative habitable zone of its star (Dittmann et al. 2017; Kane 2018). While recent ground-based observations were not precise enough to constrain atmospheric scenarios (Diamond-Lowe et al. 2020), reconnaissance with HST WFC3 shows modulation in the transit depth over the $1.1\text{--}1.7 \mu\text{m}$ wavelength range. We present atmospheric models that could fit this data but also show that stellar spot contamination can provide reasonable fits to the spectrum.

2. Data Analysis

2.1. Reduction and Analysis of Hubble Data

Our analysis started from the raw spatially scanned spectroscopic images which were obtained from the Mikulski Archive

³ These authors contributed equally to this work.

for Space Telescopes.⁴ Two transit observations of LHS 1140b were acquired for proposal 14888 (PI: Jason Dittmann) and were taken in 2017 January and December. Both visits utilized the GRISM256 aperture, and 256×256 subarray, with an exposure time of 103.13 s which consisted of 16 up-the-ramp reads using the SPARS10 sequence. The visits had different scan rates with $0''10 \text{ s}^{-1}$ and $0''14 \text{ s}^{-1}$ used for January and December respectively, resulting in scan lengths of $10''9$ and $15''9$.

We used Iraclis,⁵ a specialized, open-source software for the analysis of WFC3 scanning observations (Tsiaras et al. 2016b) and the reduction process included the following steps: zero-read subtraction, reference pixel correction, nonlinearity correction, dark current subtraction, gain conversion, sky-background subtraction, flat-field correction, and corrections for bad pixels and cosmic rays. For a detailed description of these steps, we refer the reader to the original Iraclis paper (Tsiaras et al. 2016b).

Although two transits of LHS 1140 b were obtained, one of these was affected due to large shifts in the location of the spectrum on the detector. These changes in position are shown in Figure 1 and, when the white light curve was extracted, large spikes were seen in the flux as shown in Figure 2. The presence of such shifts are known to dominate the systematics and reduce precision if the position of the spectrum is not well known (e.g., Stevenson & Fowler 2019; Tsiaras & Ozden 2019). We attempted to remove the bad frames but still could not recover a satisfactory fit. Additionally, exposures that seemed to give reasonable data in the extracted white light curve also showed obvious degradation when the fits files were visually inspected, potentially due to an unusually high number of cosmic-ray impacts. Figure 3 displays an example raw image from each data set and the degradation is easily visible for the January observation. We therefore discarded the initial observation and so only the December data set was utilized.

For this observation, the reduced spatially scanned spectroscopic images were then used to extract the white (from $1.1\text{--}1.7 \mu\text{m}$) and spectral light curves. The spectral light-curve bands were selected such that the signal-to-noise ratio (S/N) is approximately uniform across the planetary spectrum. We then discarded the first orbit of each visit as they present stronger wavelength-dependent ramps, and the first exposure after each buffer dump as these contain significantly lower counts than subsequent exposures (e.g., Deming et al. 2013; Tsiaras et al. 2016b).

We fitted the light curves using our transit model package PyLightcurve (Tsiaras et al. 2016a) which utilizes the Markov Chain Monte Carlo (MCMC) code ecme (Foreman-Mackey et al. 2013) and, for the fitting of the white light curve, the only free parameters were the mid-transit time and planet-to-star ratio. The other planet parameters were fixed to the values from Ment et al. (2019; $a/R_* = 95.34$, $i = 89^\circ.89$) while the limb-darkening coefficients were computed using the formalism from Claret et al. (2012, 2013) and the stellar parameters from Ment et al. (2019; $T_* = 3216 \text{ K}$, $\log(g) = 5.0$).

It is common for WFC3 exoplanet observations to be affected by two kinds of time-dependent systematics: the long-term and short-term ramps. These systematics were fitted

using

$$R_w(t) = n_w^{\text{scan}}(1 - r_a(t - T_0))(1 - r_{b_1}e^{-r_{b_2}(t-t_0)}), \quad (1)$$

where t is time, n_w^{scan} is a normalization factor, T_0 is the mid-transit time, t_0 is the time when each HST orbit starts, r_a is the slope of a linear systematic trend along each HST visit, and (r_{b_1}, r_{b_2}) are the coefficients of an exponential systematic trend along each HST orbit. The normalization factor we used (n_w^{scan}) was changed to n_w^{for} for upward scanning directions (forward scanning) and to n_w^{rev} for downward scanning directions (reverse scanning). The reason for using different normalization factors is the slightly different effective exposure time due to the known upstream/downstream effect (McCullough & MacKenty 2012).

We fitted the white light curve using the formulae above and the uncertainties per pixel, as propagated through the data reduction process. However, it is common in HST WFC3 data to have additional scatter that cannot be explained by the ramp model. For this reason, we scaled up the uncertainties in the individual data points, for their median to match the standard deviation of the residuals, and repeated the fitting, which is the standard practice for the Iraclis code (e.g., Tsiaras et al. 2018; Skaf et al. 2020).

Next, we fitted the spectral light curves with a transit model (with the planet-to-star radius ratio being the only free parameter) along with a model for the systematics (R_λ) that included the white light curve (divide-white method; Kreidberg et al. 2014)) and a wavelength-dependent, visit-long slope (Tsiaras et al. 2018) parameterized by

$$R_\lambda(t) = n_\lambda^{\text{scan}}(1 - \chi_\lambda(t - T_0))\frac{LC_w}{M_w}, \quad (2)$$

where χ_λ is the slope of a wavelength-dependent linear systematic trend along each HST visit, LC_w is the white light curve, and M_w is the best-fit model for the white light curve. Again, the normalization factor we used, (n_λ^{scan}), was changed to (n_λ^{for}) for upward scanning directions (forward scanning) and to (n_λ^{rev}) for downward scanning directions (reverse scanning).

The white light-curve fit is shown in Figure 4 and the subsequent spectral light-curve fits are shown in Figure 5. A full list of stellar and planet parameters used in this study is given in Table 1 while the limb-darkening coefficients and extracted spectrum are in Table 2.

2.2. Atmospheric Modeling

The retrieval of the transmission spectra was performed using the publicly available retrieval suite TauREx 3 (Al-Refaie et al. 2019).⁶ We included the molecular opacities from the ExoMol database (Tennyson et al. 2016), the high-resolution transmission molecular absorption database (HITRAN; Gordon et al. 2016), and the the high-temperature molecular spectroscopic database (HITEMP; Rothman et al. 2010) for H_2O (Polyansky et al. 2018), CH_4 (Yurchenko & Tennyson 2014), CO (Li et al. 2015), CO_2 (Rothman et al. 2010), and NH_3 (Yurchenko et al. 2011). On top of this, we also included collision-induced absorption (CIA) from $\text{H}_2\text{--H}_2$ (Abel et al. 2011; Fletcher et al. 2018) and $\text{H}_2\text{--He}$ (Abel et al. 2012) as well as Rayleigh scattering for all molecules. The priors used

⁴ <https://archive.stsci.edu/hst/>

⁵ <https://github.com/ucl-exoplanets/Iraclis>

⁶ https://github.com/ucl-exoplanets/TauREx3_public

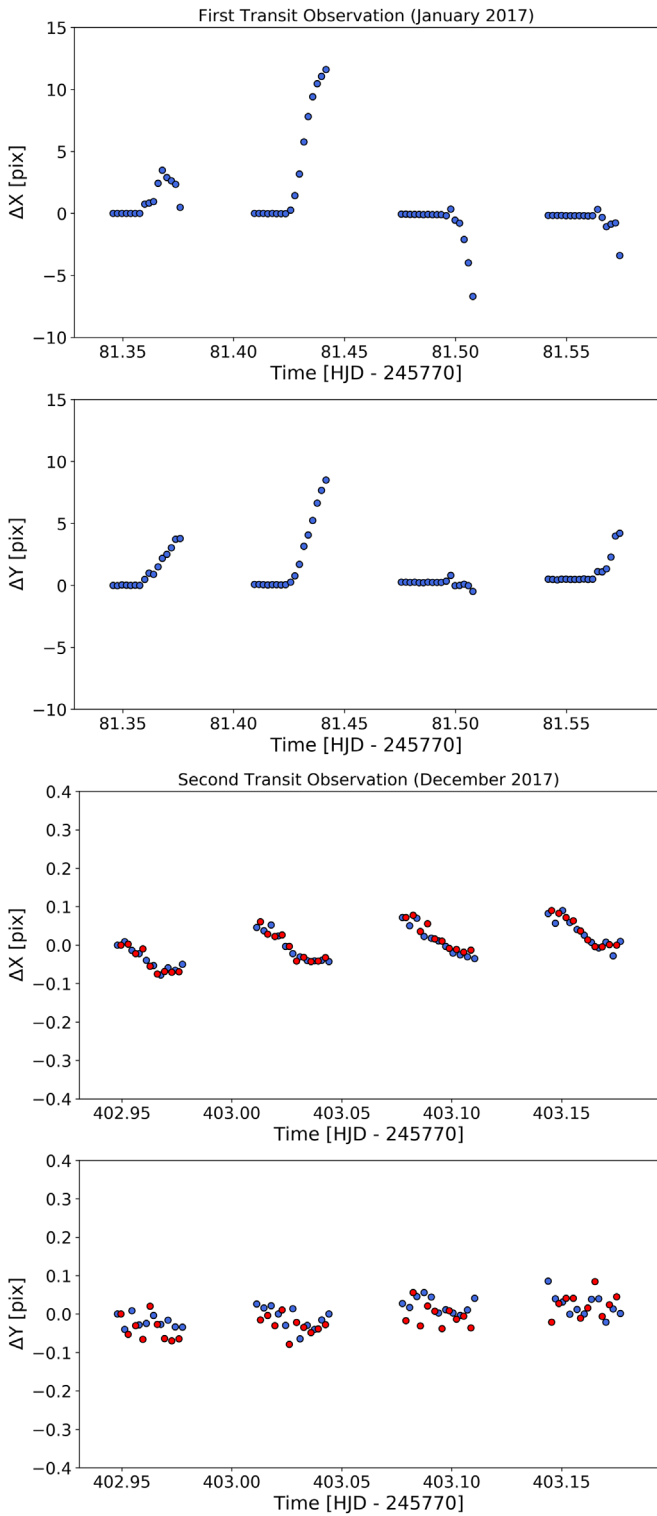


Figure 1. Shifts in the X and Y location of the spectrum for both observations. Black points indicate the forward scans while the reverse scans are shown in red.

are listed in Table 3. We allowed the bounds on the volume mixing ratio (VMR) of each molecular species to vary from 1 to $1e^{-12}$, allowing for both low and high mean molecular weight atmospheres. Our retrievals used 500 live points with an evidence tolerance of 0.5 and all retrievals for this study were performed on a single core of a 2017 MacBook Pro.

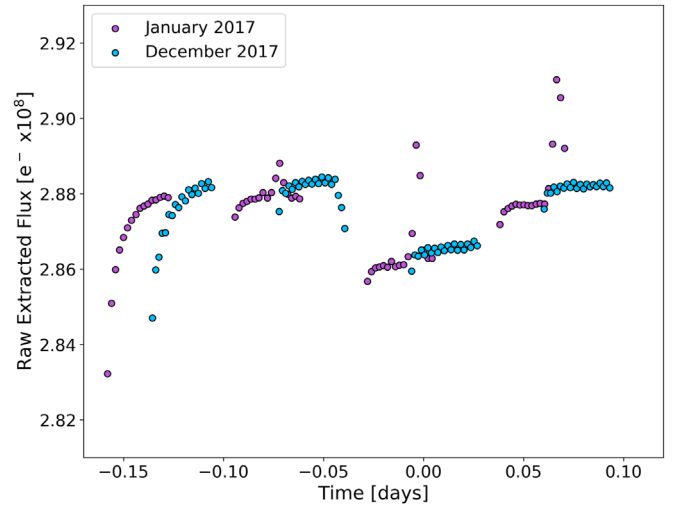


Figure 2. Raw extracted light curves for the LHS 1140b observations. Even after removing obviously bad data from the January visit, a good fitting could not be achieved so the observation was discarded. We also note that the January visit did not include reverse scans while the December observation used both forward and reverse scans. Additionally, the visits had different scan rates and thus resulted in different scan lengths on the detector.

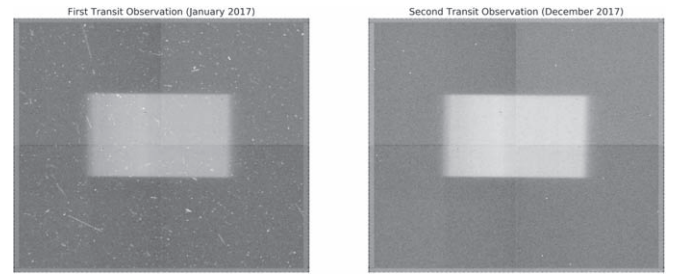


Figure 3. Example raw image from the first (left) and second (right) observations of LHS 1140b from Proposal 14888. The degradation is clearly visible in the left-hand image and was present for much of that visit.

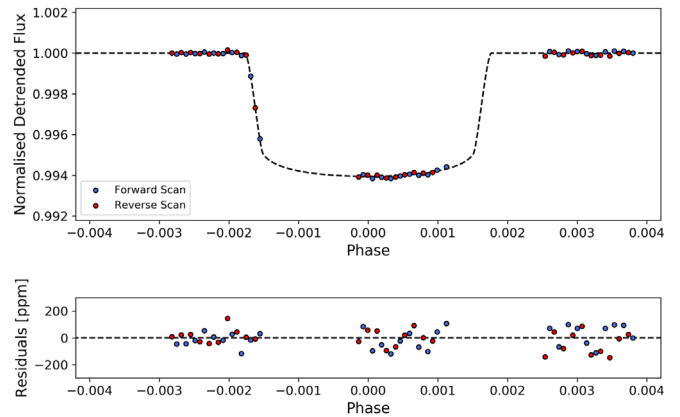


Figure 4. White light-curve fit for the December visit of LHS 1140b. Top: detrended flux and best-fit model; bottom: residuals from the best-fit model.

2.3. Modeling the Effect of Stellar Spots

We calculated the potential effect of the stellar spots on the transmission spectrum using the model from Rackham et al. (2018). LHS 1140 is known to have $\sim 1\%$ stellar brightness variability with a period of 131 days at optical wavelengths (Dittmann et al. 2017). Assuming that the variability is caused

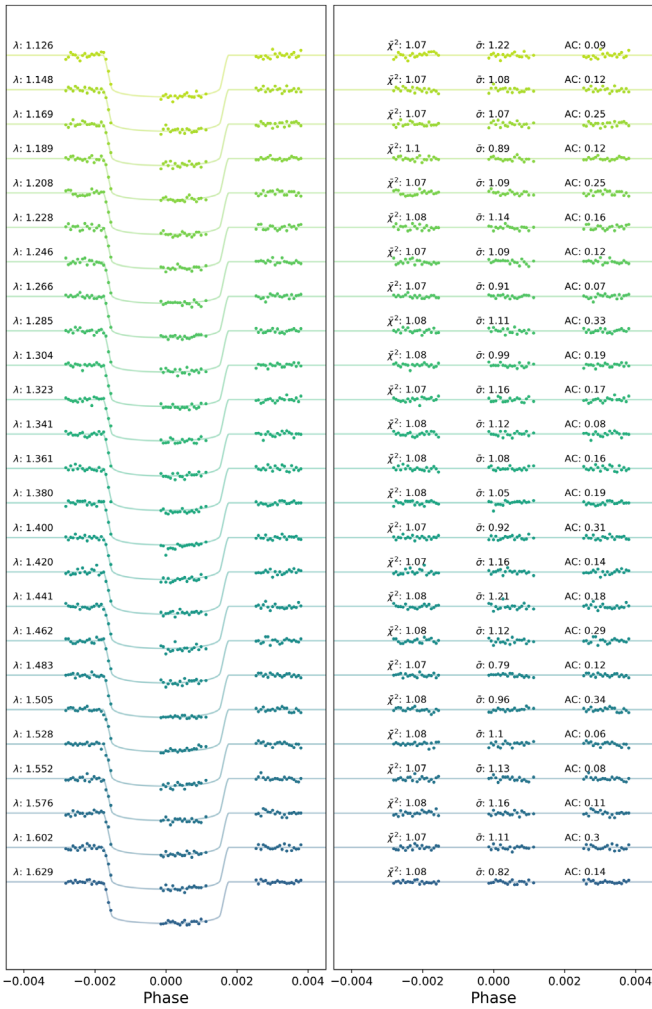


Figure 5. Spectral light-curve fits from Iraclis for the transmission spectra of LHS 1140b where, for clarity, an offset has been applied. In each plot, left panel: the detrended spectral light curves with best-fit model plotted; right panel: residuals from the fitting with values for the chi-squared (χ^2), the standard deviation with respect to the photon noise ($\bar{\sigma}$), and the autocorrelation (AC).

by stellar rotation, we infer that the stellar surface is not homogeneous. We adopted four cases of the stellar spot distribution: giant spots, solar-type spots, giant spots with faculae, and solar-type spots with faculae. These are depicted in Figure 6 and the spot covering fraction values for each case are imported from the values for M4 stars in Rackham et al. (2018), as the stellar effective temperature and brightness variability are very similar to the values from their study.

In Rackham et al. (2018), they calculate the total stellar flux by iteratively adding spots to random locations and derive the best spot covering fraction that represents a 1% variation in brightness. Note that the amplitude of the brightness variability is not proportional to the spot covering fraction, since the size of each spot is defined ($R_{\text{spot}} = 2^\circ$ for solar-like spots and $R_{\text{spot}} = 7^\circ$ for giant spots), and multiple spots are distributed over the stellar surface in all cases. We assumed the photosphere to be at 3100 K, a spot temperature of 2700 K, and faculae with temperatures of 3200 K. We used theoretical BT-Settl models of the stellar flux⁷ calculated for each

⁷ <http://svo2.cab.inta-csic.es/theory/>

Table 1
Stellar and Planetary Parameters Used or Derived in This Work

Parameter	Value
R.A. [J2000]	00 ^h 44 ^m 59 ^s .3
decl. [J2000]	−15° 1′ 18″
K_S	8.821 ± 0.024
$R_s (R_\odot)$	0.2139 ± 0.0041
$M_s (M_\odot)$	0.179 ± 0.014
T_s (K)	3216 ± 39
log(g)	5.0
Fe/H	−0.24 ± 0.10
R_p/R_s	0.07390 ± 0.00008
$M_p (M_\oplus)$	6.98 ± 0.89
$R_p (R_\oplus)$	1.727 ± 0.032
ρ (ms^{-2})	7.5 ± 1.0
g (ms^{-2})	23.7 ± 2.7
T_{eff} (K)	235 ± 5
$S (S_\oplus)$	0.503 ± 0.030
a (au)	0.0936 ± 0.0024
a/R_s	95.34 ± 1.06
i (deg)	89.89 ^{+0.05} _{−0.03}
e	< 0.06*
P_{orb} (days)	24.7369148 ± 0.0000058 [†]
T_{mid} [BJD _{TDB}]	2457187.81760 ± 0.00012 [†]
*Fixed to zero	[†] This work

Note. Data is from Ment et al. (2019) unless otherwise stated.

temperature component, at $\log g = 5$ and $[\text{Fe}/\text{H}] = 0$. The effects on the transmission spectrum at each wavelength, the contamination factor, are calculated by Equation (3) in Rackham et al. (2018). The derived contamination factor values are multiplied by a flat transit depth model, and we compared the atmospheric and stellar spots models to check which more adequately describes the observed transmission spectrum.

2.4. Transiting Exoplanet Survey Satellite Data & Ephemeris Refinement

Accurate knowledge of exoplanet transit times is fundamental for atmospheric studies. To ensure that LHS 1140b can be observed in the future, we used our HST white light-curve mid-time, along with data from the Transiting Exoplanet Survey Satellite (TESS; Ricker et al. 2014), to update the ephemeris of the planet. TESS data is publicly available through the Mikulski Archive for Space Telescopes (MAST) and we use the pipeline developed in Edwards et al. (2020) to download, clean, and fit the 2 minute cadence presearch data conditioning (PDC) light curves (Smith et al. 2012; Stumpe et al. 2012, 2014). LHS 1140b had been studied in Sector 3 and, after excluding bad data, we recovered a single transit. Again we fitted only for the transit mid-time and planet-to-star radius ratio, with all other values being fixed to those from Ment et al. (2019). For the limb-darkening coefficients we utilize the values from Claret (2017). The extracted light curve is given in Table 4 while the best-fit model is shown in Figure 7 and the mid-time, which was used for refining the ephemeris, is given in Table 5. To get the period of the planet we fitted a linear function to the observations using a least-squared fit.

Table 2
Recovered Transit Depths and Associated Errors for the HST and TESS Data Along with the Limb-darkening Coefficients Used

Wavelength (μm)	Transit Depth (%)	Error (%)	Bandwidth (μm)	a_1	a_2	a_3	a_4	Observatory
1.12625	0.5468	0.0087	0.0219	1.504	-1.434	0.903	-0.239	HST
1.14775	0.5466	0.0077	0.0211	1.465	-1.407	0.89	-0.236	HST
1.16860	0.5463	0.0075	0.0206	1.448	-1.392	0.88	-0.233	HST
1.18880	0.5464	0.0064	0.0198	1.451	-1.409	0.892	-0.237	HST
1.20835	0.5576	0.0080	0.0193	1.425	-1.364	0.859	-0.228	HST
1.22750	0.5462	0.0077	0.0190	1.381	-1.32	0.831	-0.22	HST
1.24645	0.5577	0.0078	0.0189	1.393	-1.329	0.836	-0.221	HST
1.26550	0.5466	0.0060	0.0192	1.388	-1.338	0.843	-0.223	HST
1.28475	0.5460	0.0070	0.0193	1.349	-1.294	0.814	-0.215	HST
1.30380	0.5626	0.0070	0.0188	1.337	-1.291	0.813	-0.215	HST
1.32260	0.5576	0.0082	0.0188	1.380	-1.346	0.847	-0.224	HST
1.34145	0.5557	0.0079	0.0189	1.473	-1.263	0.731	-0.184	HST
1.36050	0.5692	0.0079	0.0192	1.550	-1.348	0.776	-0.193	HST
1.38005	0.5783	0.0079	0.0199	1.637	-1.513	0.899	-0.228	HST
1.40000	0.5569	0.0068	0.0200	1.548	-1.317	0.747	-0.184	HST
1.42015	0.5464	0.0080	0.0203	1.516	-1.21	0.656	-0.157	HST
1.44060	0.5582	0.0089	0.0206	1.520	-1.216	0.659	-0.158	HST
1.46150	0.546	0.0075	0.0212	1.495	-1.195	0.651	-0.157	HST
1.48310	0.5548	0.0058	0.0220	1.499	-1.199	0.650	-0.156	HST
1.50530	0.5349	0.0071	0.0224	1.525	-1.266	0.697	-0.169	HST
1.52800	0.5463	0.0072	0.0230	1.505	-1.254	0.696	-0.170	HST
1.55155	0.5576	0.0073	0.0241	1.484	-1.244	0.694	-0.170	HST
1.57625	0.5470	0.0073	0.0253	1.502	-1.296	0.727	-0.178	HST
1.60210	0.5460	0.0074	0.0264	1.493	-1.322	0.751	-0.185	HST
1.62945	0.5462	0.0055	0.0283	1.481	-1.371	0.801	-0.200	HST
1.38400	0.5520	0.0039	0.5920	1.463	-1.302	0.766	-0.194	HST (White)
0.8	0.5116	0.0334	0.4	3.222	-4.915	4.330	-1.451	TESS

Table 3

List of the Retrieved Parameters, Their Uniform Prior Bounds, and the Scaling Used

Parameters	Prior Bounds		Scale
V_x	-12	0	\log_{10}
T_{term} (K)	50	500	Linear
P_{clouds}	6	-4	\log_{10}
R_p (R_{jup})	0.123	0.185	Linear

Note. The VMRs, denoted V_x for a given molecule x , of all retrieved molecules were permitted to range up to 100% of the atmospheric composition to search for evidence of a secondary atmosphere. Other parameters, such as the planet mass, were fixed to the values in Table 1.

3. Results

3.1. Atmospheric Retrievals

The recovered spectrum is given in Table 2 and while we ran atmospheric retrievals searching for a number of molecules, the only one for which the data supported any evidence for was H_2O . The best-fit spectrum is shown in Figure 8 while Figure 9 displays the posteriors of the H_2O -only retrieval, which suggest an abundance of $\log_{10}(V_{\text{H}_2\text{O}}) = -2.94^{+1.45}_{-1.49}$. However, we note that the significance of the detection is relatively low. We compared the Bayesian log evidence ($\log(E)$) for this retrieval to one which contained no molecular opacities. For this second retrieval the only fitted parameters were the planet radius, planet temperature, and cloud-top pressure. Rayleigh scattering

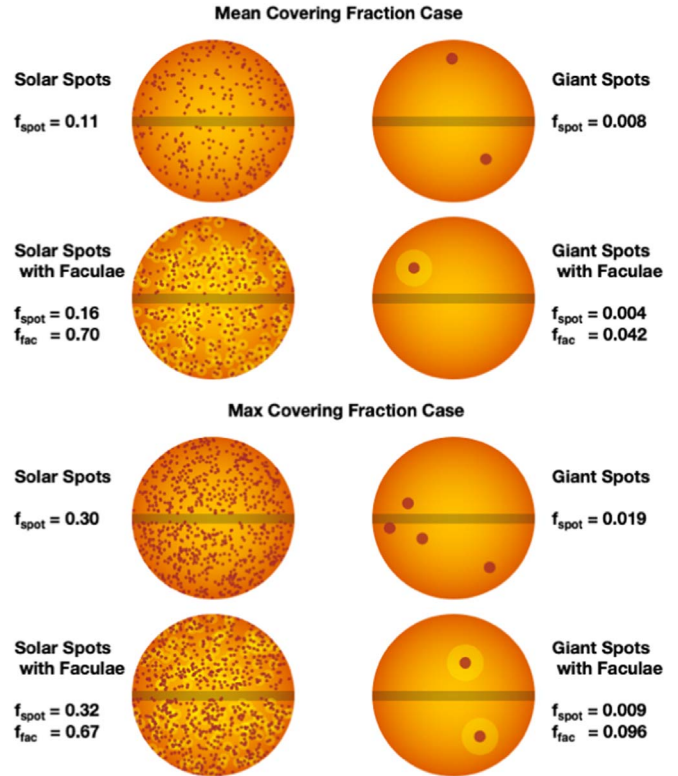


Figure 6. Graphical representation of the spot covering fractions considered in the work.

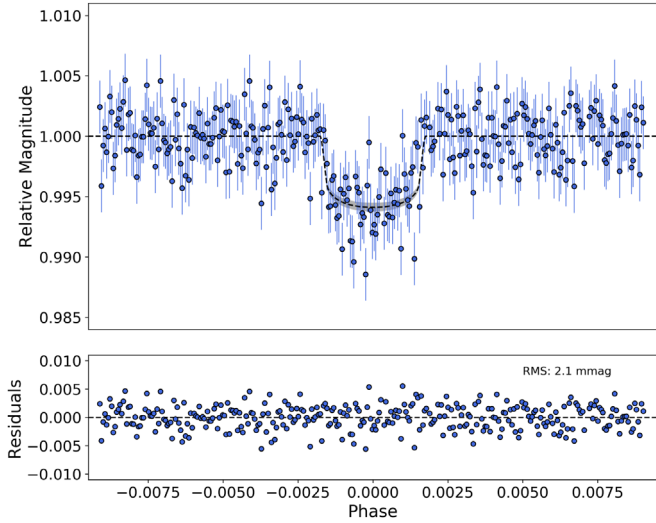


Figure 7. Fitting of TESS light curves from LHS 1140b. Left: detrended light curves and the best-fit model. Right: residuals from the fitting.

Table 4
Extracted TESS PDC Light Curve

Time [BJD _{TDB}]	Normalized Flux	Error
2458399.705274	1.002415	0.002193
2458399.706663	0.995884	0.002188
2458399.708051	0.999221	0.002191
...
2458400.151098	0.996823	0.002189
2458400.152487	1.002404	0.002194
2458400.153876	1.001115	0.002191

Note. The full table is available in a machine-readable format from the online journal. A portion is shown here for guidance.

Table 5
Transit Mid-times of LHS 1140b Used in the Ephemeris Refinement

Epoch	Mid-time [BJD _{TDB}]	Reference
-6	2456915.71154 ± 0.00004	Ment et al. (2019)
42	2458103.083434 ± 0.000073	This work
54	2458399.930786 ± 0.001305	This work

and CIA were also included. The difference in Bayesian log evidence was computed to be 2.26 in favor of the fit including H₂O, providing positive evidence for the detection of molecular features (Kass & Raftery 1995). This is equivalent to the atmospheric detectability index (ADI), as defined in Tsiaras et al. (2018), or 2.65σ.

We note that the bounds used, which are given in Table 3, allow for higher mean molecular weight atmospheres, dominated by water, but the retrieval did not favor such a solution. Nevertheless, given the debate around the nature of such planets, we also attempted a retrieval which forced an atmosphere with a significant abundance of water (>10%), with the subsequent posteriors shown in Figure 10. In the baseline retrieval, the mean molecular weight was inferred to be 2.31^{+0.28}_{-0.00}, while this second case gives a value of 6.59^{+5.73}_{-2.13} due to the VMR of water being retrieved, to 1σ, as between 13.8% and 65.6%. The forced retrieval does, in fact, give a marginally better fit to the data (log(*E*) = 195.21 versus

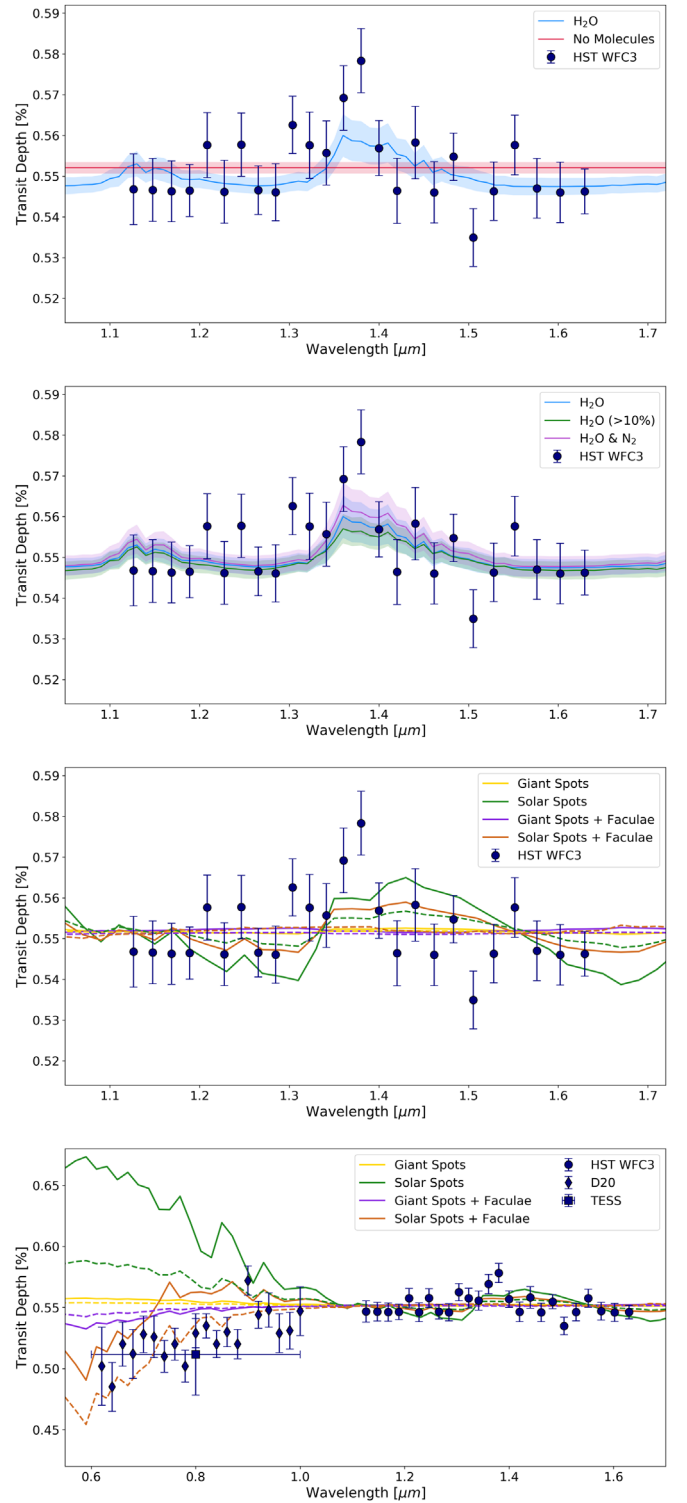


Figure 8. Best-fit models to the HST data from our atmosphere retrievals (top and upper-middle) and stellar contamination models (lower-middle). For the stellar contamination models, the solid lines depict the transit light source effect for the maximum spot filling factor, as defined in Rackham et al. (2018), while the dashed lines represent the mean. Transit depths from Diamond-Lowe et al. (2020) are also shown (bottom) and suggest the presence of solar spots with faculae.

log(*E*) = 194.47) and, compared to the flat model, is preferred by 2.95σ. However, given the small difference in evidence between the two retrievals including water, and that the Bayesian evidence is sensitive to the prior, one cannot use

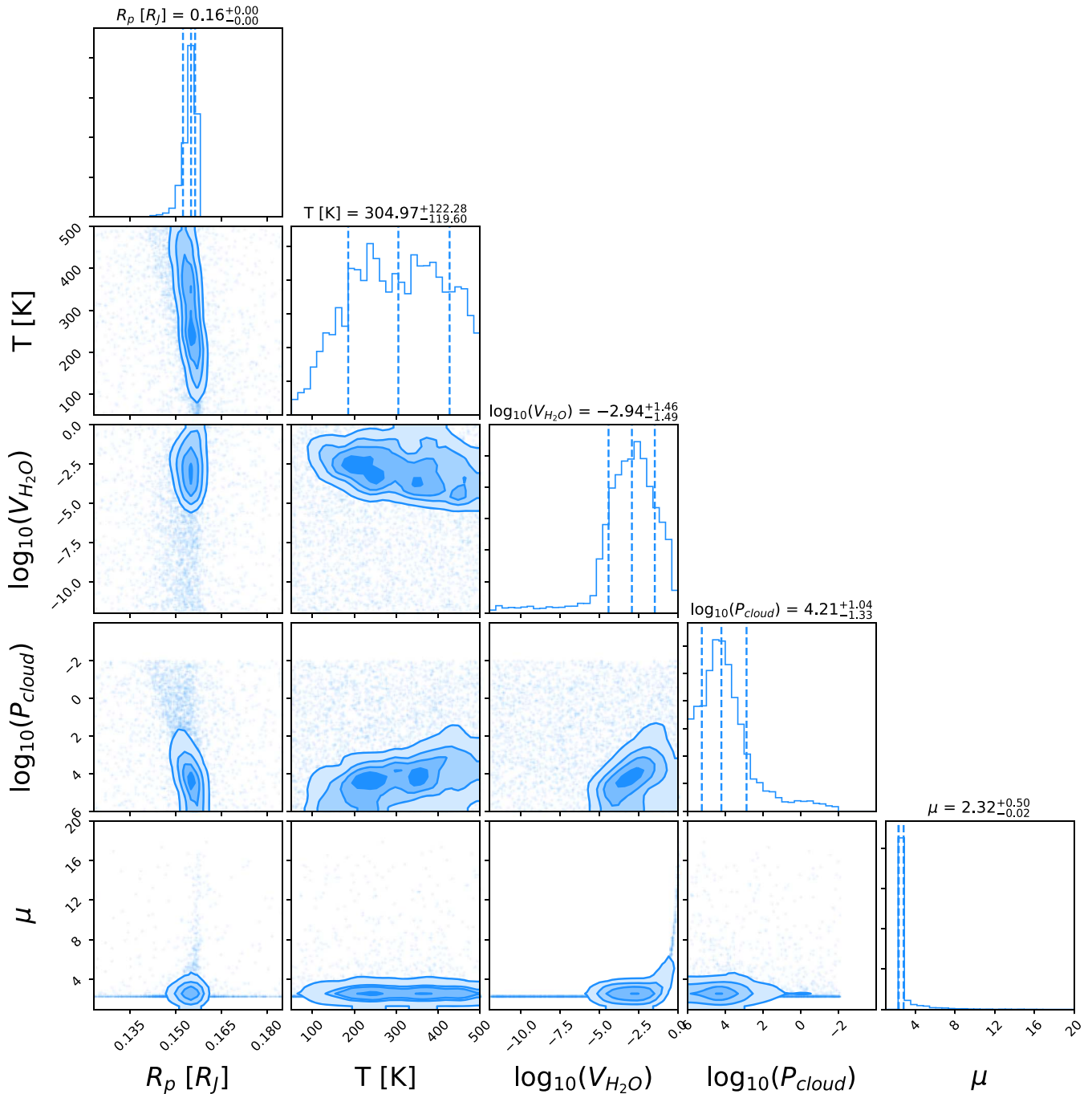


Figure 9. Posterior distributions for the water-only atmospheric retrieval of LHS 1140b. The water probability distribution is well defined and the mean molecular weight indicates a primary atmosphere.

statistical means to preferentially select either (Kass & Raftery 1995).

As in Tsiaras et al. (2019), we also performed a retrieval which included nitrogen to increase the mean molecular weight without adding additional molecular absorption features. In this case, a water abundance of $\log_{10}(V_{\text{H}_2\text{O}}) = -2.96^{+1.49}_{-1.73}$ was recovered while the N_2/H_2 ratio was best fit as $-4.75^{+3.22}_{-3.42}$, as shown in Figure 11. The Bayesian evidence ($\log(E) = 192.51$) is again similar to the other models. Hence, while all our retrievals point to the presence of water, the nature of the atmosphere (i.e., primary or secondary) cannot be ascertained. Additionally, while comparing the Bayesian evidence from

different retrievals that favor those with water, the difference in the evidence in all of the cases is small and it is worth noting that, compared to the flat model, the water-only retrieval has but a single additional fitting parameter ($\log_{10}(V_{\text{H}_2\text{O}})$). The water opacity adds great freedom to the model to fit the modulation without overly penalizing the resulting Bayes factor for this increase dimensionality. For completeness, we also report the results of two retrievals with H_2O , NH_3 , CH_4 , CO , and CO_2 as active absorbers: one where all molecules could form up to 100% of the atmosphere and a second where all but water were capped at 10%. These resulted in water abundances of $\log_{10}(V_{\text{H}_2\text{O}}) = -3.31^{+1.93}_{-4.11}$ and $-3.74^{+1.80}_{-4.39}$, respectively, with evidences of $\log(E) = 194.51$ and 194.33 . Again positive

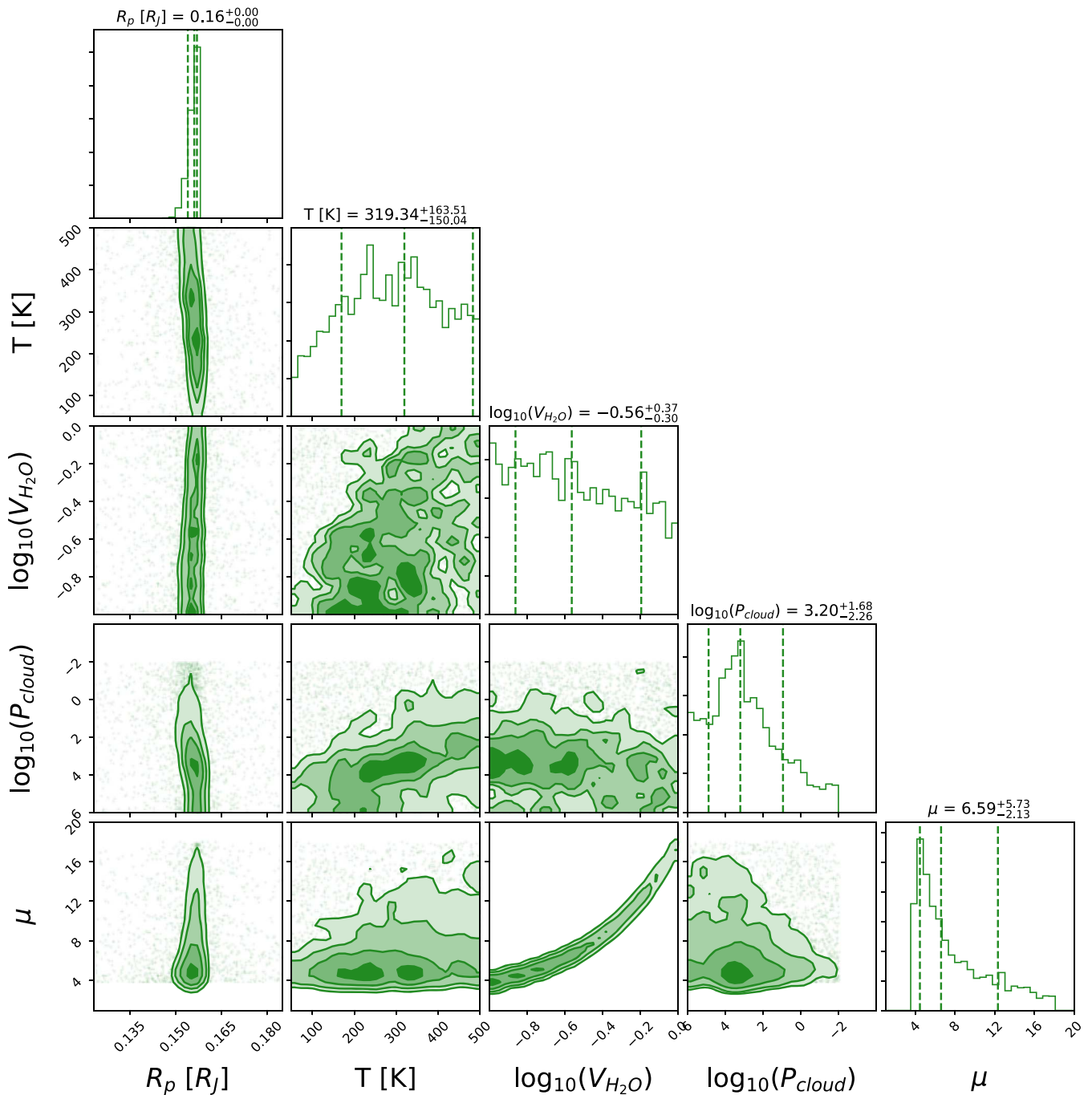


Figure 10. Posterior distributions for the water-only atmospheric retrieval of LHS 1140b where the water abundance is forced to be >10%. The probability distribution of water is flat and the mean molecular weight highlights the shift toward a heavier atmosphere which is forced by this retrieval.

evidence is found for atmospheric features but, in the latter case, the significance of the detection is reduced: the dimensionality of the fit has increased but the quality of it has not. Hence, while comparing the evidence from models is crucial, it must be done cautiously, with an understanding of the underlying statistical implications and the effects of the choice of one’s priors: fine tuning one’s priors can lead to apparent increases or decreases in the significance of a detection.

3.2. Stellar Contamination

The models of potential contamination are also plotted in Figure 8. For each, we compute the chi-squared as a means of

comparing the ability of the model to fit the data. We additionally used the same metric to analyze the fit of the models from our retrievals. For simplicity, we chose to only compare the flat model and primary atmosphere containing water. As shown in Table 6, the preferred case is still an atmosphere containing H₂O. We note that none of the starspot models alone provide convincing fits to the data, with the features induced coming at longer wavelengths and being broader than those seen in the data.

Spectroscopic ground-based observations of LHS 1140b were recently presented by Diamond-Lowe et al. (2020). They observed two transits of the planet and simultaneously monitored them with the IMACS and LDSS3C multi-object

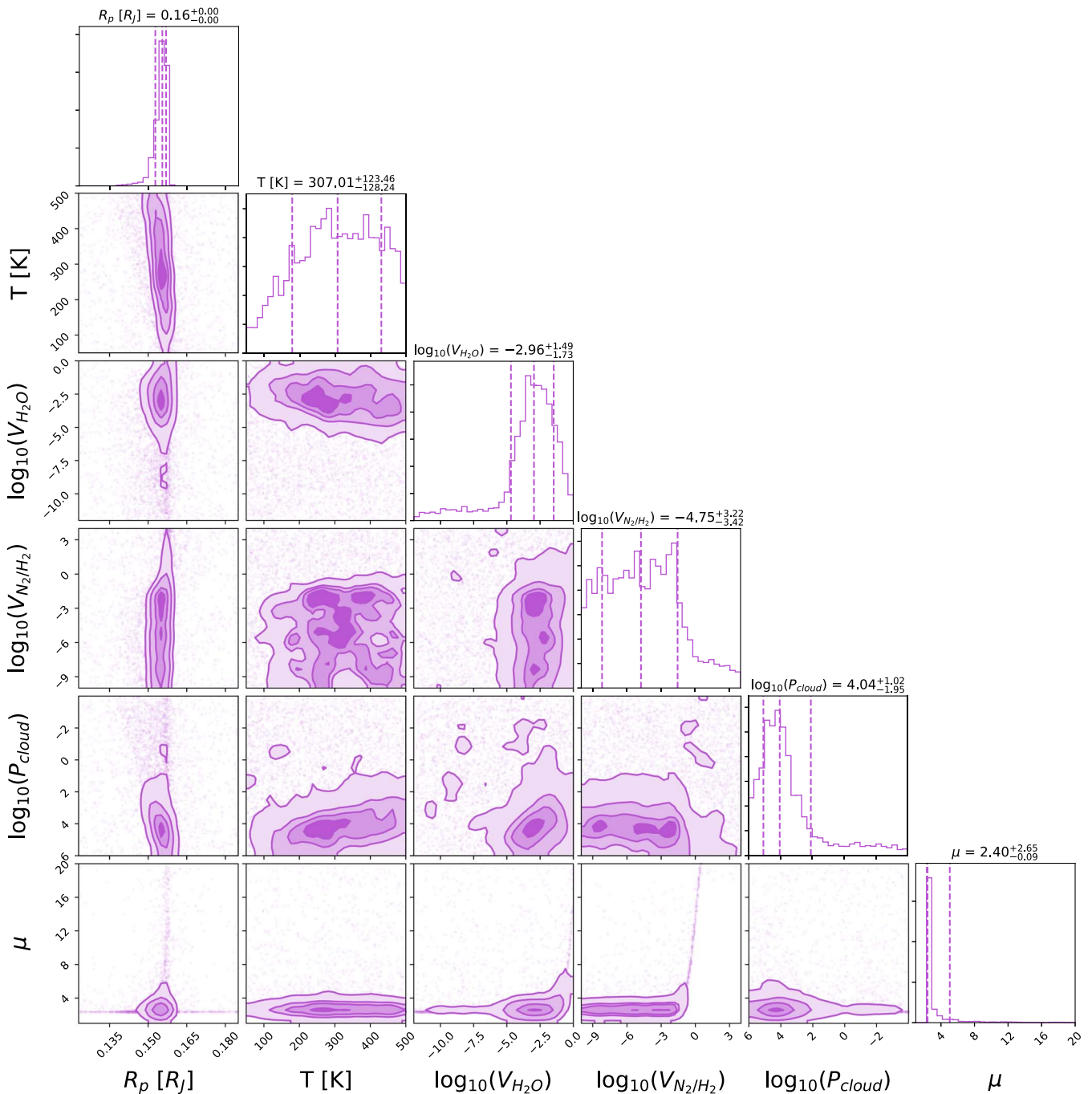


Figure 11. Posterior distributions for the retrieval where, alongside the water abundance, the nitrogen-to-hydrogen ratio was fitted. The retrieved water abundance is highly similar to that in Figure 9.

spectrographs on the twin Magellan telescopes. Their spectroscopic measurements resulted in a spectrum with a median error of 260 ppm which is significantly larger than the ~ 70 ppm achieved here.

We note that the compatibility of different data sets is hard to confirm, particularly without spectral overlap, as the use of different limb-darkening coefficients or orbital parameters, imperfect correction of instrument systematics, or stellar activity and stellar variability can all cause variations in the transit depth observed (e.g., Tsiaras et al. 2018; Alexoudi et al. 2018; Yip et al. 2020a, 2020b; Changeat et al. 2020; Pluriel et al. 2020). Diamond-Lowe et al. (2020) used the same orbital parameters, from Ment et al. (2019), but used logarithmic

limb-darkening coefficients. However, the TESS depth recovered here matches well with the ground-based data and was derived using the four-coefficient law from Claret (2017). In Figure 8, the data from Diamond-Lowe et al. (2020) is plotted alongside the HST and TESS transit depths recovered here.

The ground-based data set appears to show a shallower transit depth than any of the stellar contamination models but the solar spots with the faculae model provide the best fit as demonstrated by the chi-squared values in Table 7. The plotted data in Figure 8 assumes no offsets between data sets but, to ensure we do not draw false conclusions because of one, we renormalize the stellar contamination models. To do this we sample various offsets for each stellar model, finding the

Table 6Chi-squared (χ^2) and Reduced Chi-squared ($\bar{\chi}^2$) Values for Different Atmospheric and Stellar Contamination Models for the HST WFC G141 Data

Model		χ^2	$\bar{\chi}^2$
Atmosphere	H ₂ O	29.48	1.40
	Flat	35.82	1.63
Giant spots	Mean	35.43	1.61
	Max	35.11	1.60
Solar spots	Mean	34.76	1.58
	Max	51.83	2.36
Giant spots + faculae	Mean	35.86	1.71
	Max	36.05	1.72
Solar spots + faculae	Mean	33.67	1.60
	Max	34.18	1.63

Table 7

Chi-squared Values for Different Atmospheric and Stellar Contamination Models for the Data from Diamond-Lowe et al. (2020)

No Renormalization			
Model		χ^2	$\bar{\chi}^2$
Giant spots	Mean	95.43	5.61
	Max	107.45	6.32
Solar spots	Mean	239.39	14.08
	Max	840.16	49.42
Giant spots + faculae	Mean	73.82	4.61
	Max	62.67	3.92
Solar spots + faculae	Mean	30.05	1.88
	Max	120.6	7.54
With Renormalization			
Giant spots	Mean	33.8	1.99
	Max	36.0	2.12
Solar spots	Mean	61.11	3.59
	Max	186.8	10.99
Giant spots + faculae	Mean	29.15	1.82
	Max	25.74	1.61
Solar spots + faculae	Mean	28.09	1.76
	Max	34.1	2.13

best-fit value using the chi-squared metric. These are shown in Figure 12 and the chi-square values are again given in Table 7.

Given the downward slope seen in this data set, this would appear to rule out the case of solar spots without faculae, which would provide the largest modulation in the HST wavelength range. Of the stellar models computed, before renormalization the mean coverage of solar spots with faculae provides the best fit to the slope seen in this ground-based data set: the same model also best fits the HST data. After renormalization, solar spots and faculae in both coverage cases give a reasonable fit. Additionally, giant spots and faculae, with either mean or maximum coverage, also provide good fits to the IMACS/LDSS3C data set and these do not cause modulation in the WFC3 bandpass.

3.3. Impact of Accounting for Stellar Contamination

Of course, one would not expect the spectrum to be explained entirely by the stellar model unless LHS 1140b were to have no atmosphere. Hence, the signal seen should be a combination of contributions. To explore the effect of stellar contamination on the retrieved atmosphere, and thus the significance of the water detection, we tested subtracting our

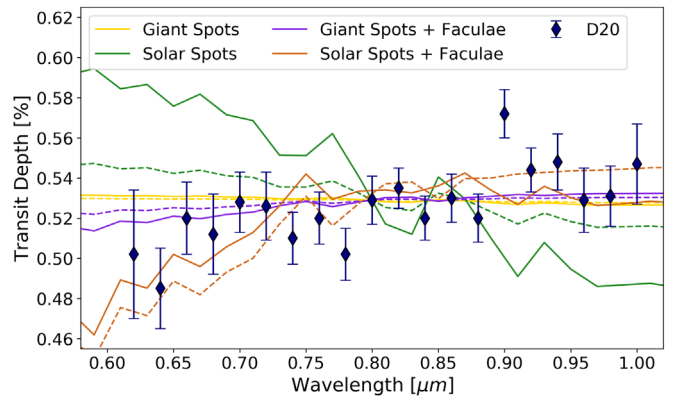


Figure 12. Stellar contamination models when renormalized to the ground-based data from Diamond-Lowe et al. (2020).

spot models from both our HST data set and the observations from Diamond-Lowe et al. (2020). The effect of stellar contamination is greater in the visible. Hence, we use this to rule out spot contamination models which would imply nonphysical atmospheric features in the data from Diamond-Lowe et al. (2020). A similar approach was taken by Wakeford et al. (2019) for TRAPPIST-1 g. While a slope that increases at shorter wavelengths can be described by Rayleigh scattering, a negative one would be more difficult to describe. If solar spots were the correct contamination model, the atmospheric feature would be around 40 scale heights in the max coverage case, or 30 in the mean, and thus is not feasible. Other models still have large feature sizes, 10–20 scale heights, but the data is relatively noisy and the error bars are of the order of several scale heights.

For the HST data, we also accounted for each stellar contamination model by subtracting the contribution and conducting two retrievals on the resultant spectrum: one with water and one without. The only three models which cause significant modulation in the HST WFC3 bandpass are solar spots, both mean and max coverage, and the max coverage of solar spots with faculae. Subtracting each of these essentially completely removed any evidence for water in the atmosphere. However, as mentioned, the visible data could not be explained in the solar spots case. Plots of the subsequent HST WFC3 data, with best-fit models, are given in Figure 13. The corrected spectrum in the max solar spots case is strange and the retrieval tries to use CIA to explain the modulation. The maximum coverage of solar spots and faculae is the only stellar contamination model which leads to no evidence for water in the atmosphere of LHS 1140b and is not ruled out by the visible data.

Having accounted for all other models, our retrievals still favored the presence of water with a confidence of $2.38\text{--}2.77\sigma$ and with an abundance similar to that from our baseline retrieval on the unmodified HST data, as shown in Table 8.

3.4. Impact of Removing Data Points and Different Limb-darkening Coefficients

The spectrum obtained using HST WFC3 contains 25 data points but the evidence for water is likely to be driven by only a few of these: those around $1.4\ \mu\text{m}$ where the feature is the strongest. Therefore we attempted retrievals on data sets where we removed individual data points. Each time we ran the model with and without water and compared the difference in the

Table 8
Retrieved Water Abundance after Accounting for Different Stellar Contamination Models

Stellar Model		Water Abundance	log(E) Water	log(E) Flat	$\Delta\log(E)$	Sigma
Giant spots	Mean	$-2.85_{-1.69}^{+1.48}$	194.07	192.43	1.64	2.37
	Max	$-2.98_{-1.69}^{+1.68}$	194.17	192.51	1.66	2.38
Solar spots	Mean	$-4.31_{-4.75}^{+2.57}$	193.12	192.71	0.41	0.26
	Max	$-7.11_{-3.32}^{+3.41}$	184.30	184.50	-0.20	...
Giant spots + faculae	Mean	$-2.92_{-1.42}^{+1.51}$	194.50	192.07	2.43	2.73
	Max	$-2.78_{-1.41}^{+1.36}$	194.58	192.04	2.54	2.77
Solar spots + faculae	Mean	$-2.78_{-1.70}^{+1.43}$	195.37	193.24	2.13	2.60
	Max	$-5.57_{-4.27}^{+3.20}$	193.57	193.11	0.46	0.26
None		$-2.94_{-1.49}^{+1.45}$	194.47	192.21	2.26	2.65

Note. The Bayesian evidence for the models with and without water are also given along with the sigma level for each.

global log evidence. Our analysis found that removing the data point at $1.38 \mu\text{m}$ eliminates all indications from water being present with the removal of the $1.36 \mu\text{m}$ data point reducing the confidence to 2.01σ . Meanwhile, deducting the spectral data at 1.40 or $1.42 \mu\text{m}$ changes the confidence of the models that water is present to 2.57 and 2.9σ , respectively. Such results are expected given the narrow wavelength region means only one water feature is probed.

To further explore the quality of the spectral light-curve fitting, and thus of the water detection, we also produced a spectrum at the native resolution of the G141 grism ($R \sim 130$ at $1.4 \mu\text{m}$). A peak of several data points is seen in this data set around the $1.4 \mu\text{m}$ water feature, as seen in Figure 14, suggesting the peak seen is not due to a narrowband contamination of the spectra. Additionally, we studied the autocorrelation function of each spectral light-curve fit. Various correlations are calculated (e.g., between one point and the next) using the `numpy.correlate` package and the maximum value is reported. Figure 15 shows that the $1.38 \mu\text{m}$ data point, the one on which the water detection hinges, appears to be well fitted and thus reliable.

The choice of limb-darkening coefficients can also have profound effects on the recovered spectrum, particularly for cooler stars (e.g., Kreidberg et al. 2014), and several different limb-darkening laws are available. We attempted fits with precomputed linear, square-root, and quadratic coefficients, again calculated using ExoTETHyS (Morello et al. 1919), but only the linear values provided usable fits to the white light curve. Additionally, we fitted the data with claret coefficients for different stellar temperatures. The linear law and additional claret fits all resulted in spectra which agree with the one originally derived to within 1σ , as shown in Figure 16. Nevertheless, we performed retrievals on these spectra, finding that they preferred a solution with water to 2.98 and 2.92σ for claret coefficients at 3150 and 3250 K, respectively, while the linear coefficients resulted in a 3.22σ detection of water.

Finally, a recent study used ESPRESSO and TESS data to provide updated system parameters (Lillo-Box et al. 2020). Hence we tried fitting the light curves using their parameters ($a/R_s = 96.4$, $i = 89.877^\circ$) as well as performing retrievals using their revised mass ($M_p = 6.38 M_\oplus$). The resultant spectrum, and best-fit retrieval, is shown in Figure 17. The spectrum still shows evidence for water with an abundance of $\log_{10}(V_{\text{H}_2\text{O}}) = 3.01_{-1.59}^{+1.58}$ and a significance of 2.57σ . On this alternate spectrum we also conducted a retrieval with CH_4 as the main absorber, resulting in an abundance of $\log_{10}(V_{\text{CH}_4}) = 3.37_{-5.01}^{+2.48}$, but the model did not

provide a significantly better fit than the at model ($\log(E) = 191.01$ versus $\log(E) = 190.47$).

4. Discussion

Our results for LHS 1140b prefer the presence of an atmosphere containing water vapor. However, given the noise and scatter of the signal, a flat spectrum cannot be ruled out and the primary/secondary nature of the atmosphere cannot be determined. Additionally, M dwarfs are known to be capable of creating spectral signatures which can alter the derived atmospheric composition.

Other rocky habitable-zone planets have shown a completely flat spectrum (de Wit et al. 2016, 2018; Ducrot et al. 2018; Zhang et al. 2018; Wakeford et al. 2019). The analysis of K2-18 b (Tsiaras et al. 2019; Benneke et al. 2019) suggests that the planet could have a significant amount of water vapor in the atmosphere but may also have a non-negligible fraction of hydrogen. The presence of water vapor sparked an intense debate on habitability, largely due to the size of the planet and the presence of hydrogen in the atmosphere. A similar detection in the atmosphere of LHS 1140b would have important consequences for habitability, indicating that water vapor is not a rare outcome for smaller, temperate planets. Figure 18 highlights the HST WFC3 spectra for TRAPPIST-1 e and f, the planets in system with the most similar equilibrium temperatures to LHS 1140b, as well as K2-18 b. In each case, a model for a clear primary atmosphere is overplotted with a water abundance of $\log_{10}(V_{\text{H}_2\text{O}}) = -3$. The TRAPPIST planets clearly do not possess such an atmosphere while the water feature seen on K2-18 b is far better defined than the potential one uncovered here.

Although it is larger than the TRAPPIST-1 planets, LHS 1140b has a density which is compatible with a rocky composition, predominantly composed of iron and magnesium silicates (Dittmann et al. 2017; Ment et al. 2019). Hence, the presence/absence of a hydrogen envelope around this planet would substantially inform the debate around the TRAPPIST-1 planets and K2-18 b. The relatively low level and stability of UV flux experienced by LHS 1140b should be favorable for its present-day habitability (Spinelli et al. 2019), making this planet one of the most interesting targets for the search of biosignatures in the future although Galactic cosmic rays could impact this (Herbst et al. 2020). Measurements and interior modeling by Lillo-Box et al. (2020) suggest that the planet could possess a substantial mass of water. Modeling suggests that, if it were to have a surface ocean, LHS 1140b may be in a

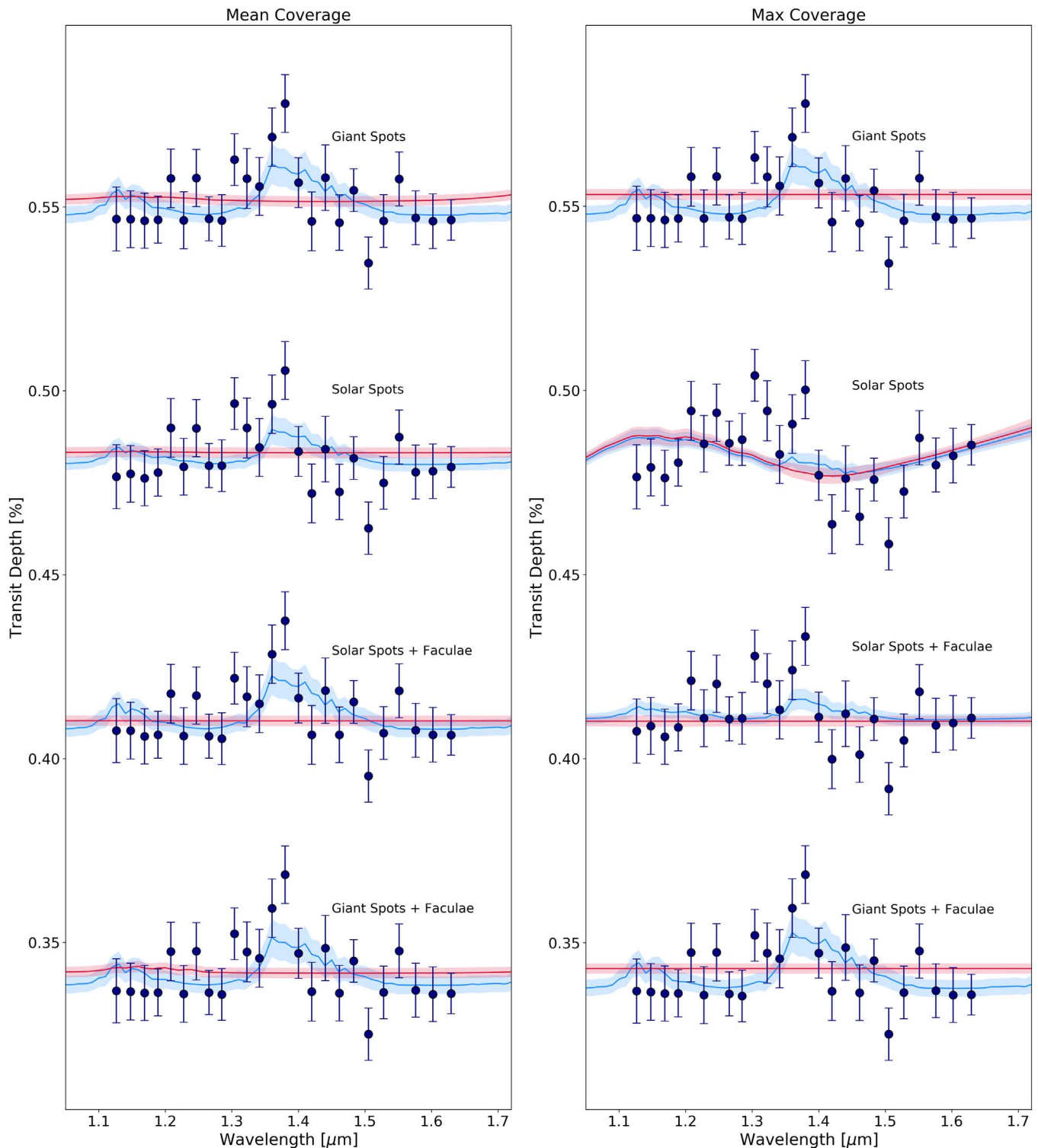


Figure 13. Corrected HST WFC3 spectrum for different stellar contamination models and the subsequent best fits from retrievals with (blue) and without (red) water. In the majority of cases, a solution with water is preferred. The modulation seen in the retrievals on the data corrected for max coverage of solar spots is due to CIA.

snowball state (Yang et al. 2020) or have a unglaciated substellar region (Checlair et al. 2017).

Confidently detecting the presence of spectroscopic signatures will allow us to differentiate between hydrogen-rich and heavier atmospheres, a key sign of the provenance and evolution of super-Earths. From a formation perspective, while in situ formation of super-Earths is theoretically possible, it

may happen only under very specific conditions (Ikoma & Hori 2012; Ogiwara et al. 2015). Current formation models predict that Neptune-mass planets or larger are forced to move to closer orbits when a critical mass is being accreted (Ida & Lin 2008; Mordasini et al. 2009; Ida & Lin 2010). Super-Earths could therefore be the remnants of larger planets which have lost part of their initial gaseous envelope, due to XUV-driven

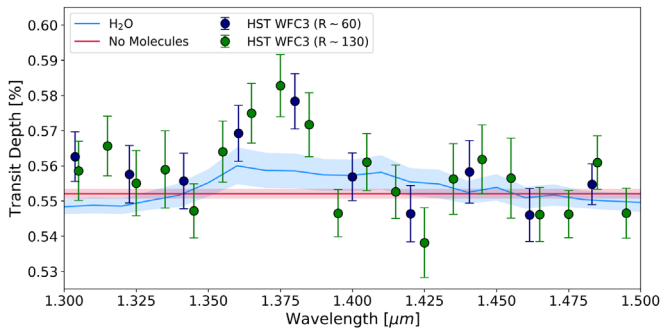


Figure 14. Higher-resolution HST WFC3 G141 spectrum plotted alongside the main spectral data set and best-fit models. The high-resolution spectrum also peaks around the water feature at 1.4 μm .

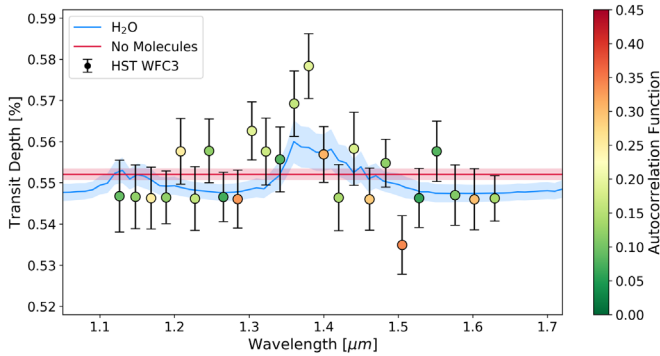


Figure 15. HST WFC3 G141 with the data points colored by value of the autocorrelation function for their fitting.

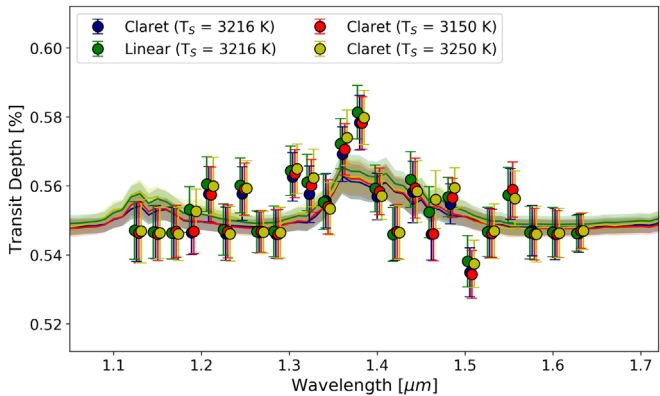


Figure 16. The spectra recovered from the fitting using different limb-darkening coefficients. They are all within 1σ of each other and, from our retrievals, prefer the presence of water to a flat model.

hydrogen mass-loss coupled with planetary thermal evolution (Leitzinger et al. 2011; Owen & Jackson 2012; Lopez et al. 2012; Owen & Wu 2013, 2017).

In this scenario planets with radii $< 1.7 R_{\oplus}$ are expected to have lost most of their primordial hydrogen envelope, while planets larger than $1.7 R_{\oplus}$ are expected to have retained at least some of it. Current observations of small, rocky worlds have not been compatible with hydrogen-dominated, cloud-free atmospheres. With a radius of $1.7 R_{\oplus}$, LHS 1140b is situated between these two populations. By being a world that unambiguously has a solid surface, the confirmation/rejection for the presence of large amount of hydrogen would significantly impact our understanding of small worlds.

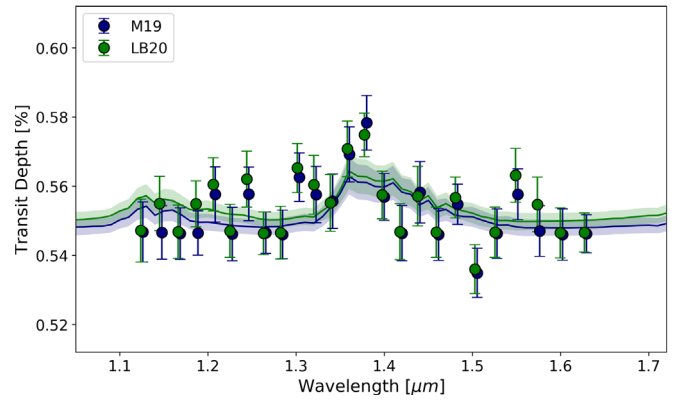


Figure 17. The spectra recovered from the fitting using different parameters from Ment et al. (2019) and Lillo-Box et al. (2020). They are within 1σ of each other and, from our retrievals, prefer the presence of water to a flat model.

Meanwhile, the potential for large amounts of water in the atmospheres of LHS 1140b and K2-18 b could hint toward the existence of water worlds (Zeng et al. 2019). Definitive constraints on the atmospheric chemistry of LHS 1140b would inform formation processes, exoplanet evolution, and interior/atmospheric models.

5. Future Observations

The confirmation/refutation of an atmospheric envelope and of a water signature of LHS 1140b will significantly guide current debates into the nature of small exoplanets, constrain planet evolution models, and inform us about the potential habitability of rocky worlds orbiting M dwarfs. A number of different space-based facilities could be utilized for this study.

First, additional HST WFC3 G141 observations could be taken. Using the errors from the data analysis here, we simulated the effect of adding two further HST observations based upon the best-fit solution and that these could increase the significance of the detection, in comparison to the flat model, to $> 5\sigma$. Figure 19 displays the spectrum recovered from HST WFC3 G141 along with several forward models for a cloudy H/He atmosphere and one with a high mean molecular weight. The addition of two new transits would decrease the average error from ~ 80 ppm to less than 50 ppm.

However, disentangling potential stellar contamination will still be difficult given the narrow wavelength coverage. Observations with the G102 grism could help by filling the spectral gap between the current HST data and that from the ground. Nevertheless, given the long baseline between observations, difficulties may still remain. Furthermore, if the atmosphere of LHS 1140b is not clear and hydrogen dominated, then distinguishing between a cloudy primary atmosphere or one with a higher mean molecular weight would be difficult with additional HST data alone.

The James Webb Space Telescope (JWST), currently scheduled for launch in late 2021, will provide unparalleled sensitivity and previous simulations have shown that H_2O , CH_4 , and CO_2 could be detected by JWST in the atmosphere of an Earth-like planet around LHS 1140 (Wunderlich et al. 2019). We simulate a single-transit observation with NIRISS GR700XD and spectrally bin the data to reduce the resolution to $R \sim 50$, as shown in Figure 19. Such a data set would allow us to confirm, or refute, the presence of a clear, H/He atmosphere around LHS 1140b as it would provide a higher S/N on the atmosphere while the wide spectral coverage will

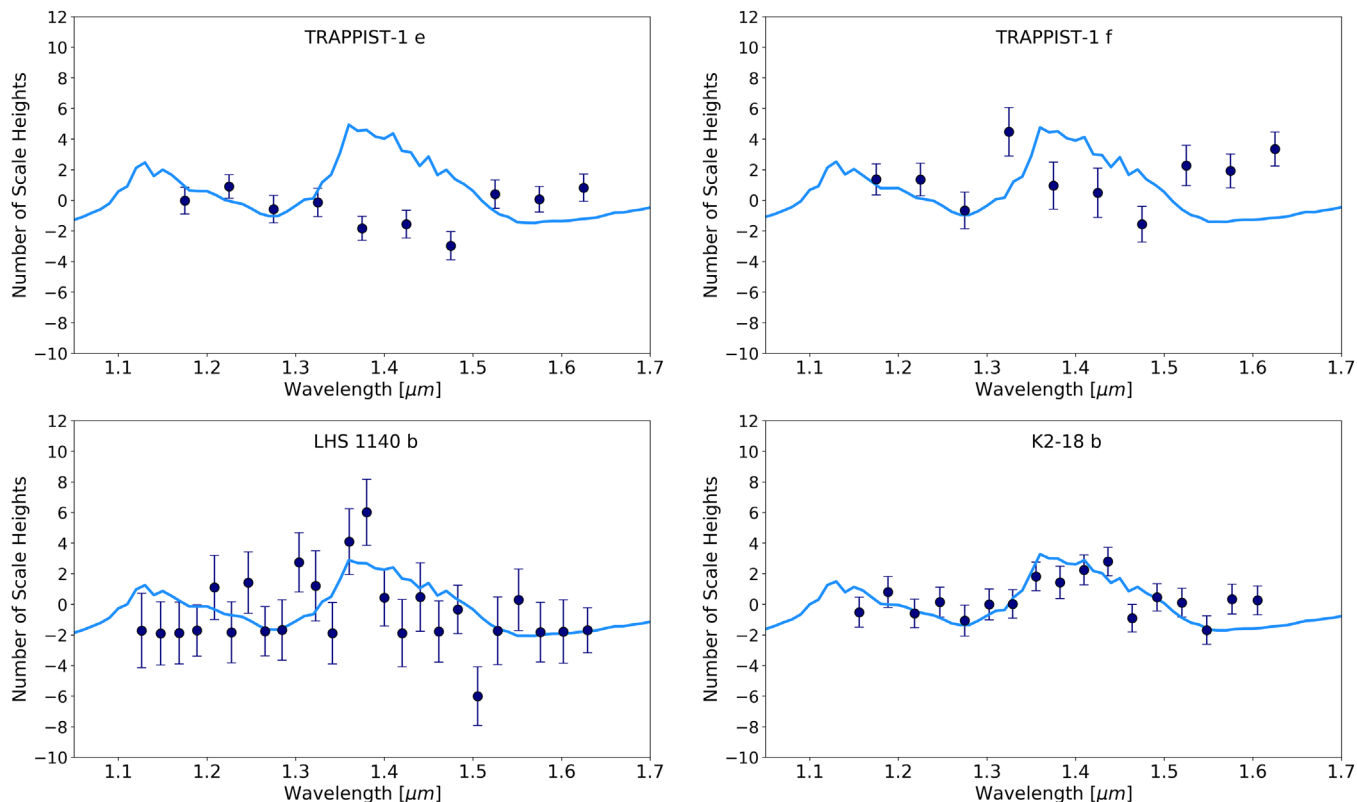


Figure 18. Comparison of the spectrum derived here for LHS 1140b and those of K2-18 b (Tsiaras et al. 2019) as well as TRAPPIST-1 e and f (de Wit et al. 2018). Overplotted for each is a forward model assuming a clear H/He-dominated atmosphere with a water abundance of $\log_{10}(V_{\text{H}_2\text{O}}) = -3$.

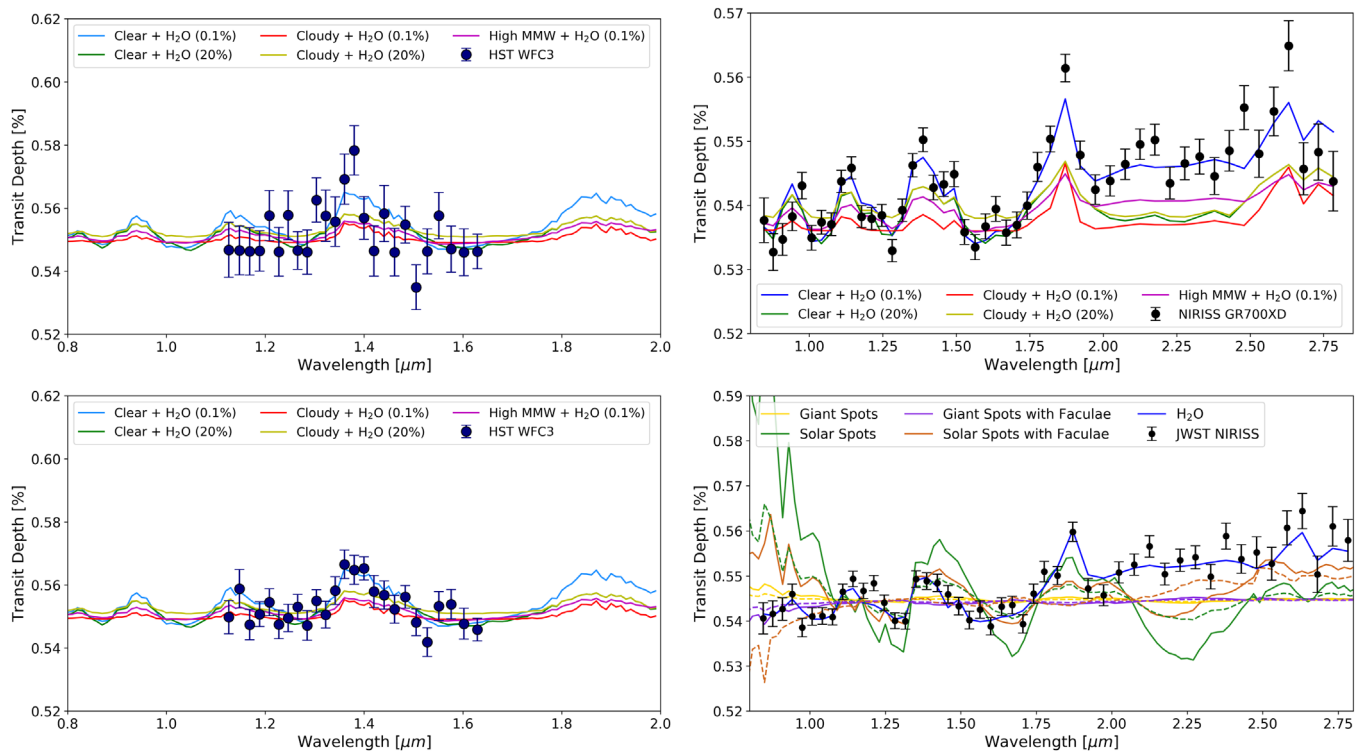


Figure 19. Upper left: transmission spectrum from the WFC3 G141 data of LHS 1140b analyzed here (black) with various forward models overplotted. The best-fit solution from an atmospheric retrieval favors the presence of a clear, H/He atmosphere with water (blue). Lower left: simulated final spectrum (black) when the current data is combined with two further HST WFC3 G141 observations, increasing the ability to confirm the presence of water. Upper right: expected data from JWST NIRISS GR700XD which suggests that these observations could provide a definitive answer to the question: does LHS 1140b have a clear, H/He-dominated atmosphere? Lower right: transit light source models for the JWST data which are heavily intertwined with the atmospheric signal, highlighting the importance of understanding this effect in the JWST era.

probe multiple bands of molecular absorption. The continuous coverage from the visible into the near-infrared would also aid in the fitting of the stellar signal. Constraining an atmosphere with a higher mean molecular weight is likely to take many more transits. Given its long period and location close to the ecliptic plane, only around four transits of LHS 1140b per year would be observable with JWST and thus initial observations should be taken as soon as possible. Observations with NIRISS GR700XD were planned as part of GTO Proposal 1201 (PI: David Lafreniere) but were withdrawn in favor of studying other planets (Lafreniere 2017).

The ESA M4 mission the Atmospheric Remote-sensing Infrared Exoplanet Large-survey (ARIEL) will survey a population of 1000 exoplanets during its primary mission (Tinetti et al. 2018) and much of this could be dedicated to studying smaller planets in, and around, the radius gap (Edwards et al. 2019). Although not modeled here, its wide, simultaneous spectral coverage (0.5–7.8 μm) will undoubtedly be useful for characterizing and removing stellar contamination, allowing an accurate recovery of the atmospheric parameters. The same is true for Twinkle, another space-based spectroscopic mission, which will simultaneously cover 0.4–4.5 μm (Edwards et al. 2019) and both these observatories are likely to be able to observe around 3–4 transits per year.

Finally, observations monitoring the star, such as those conducted for GJ 1214 (e.g., Berta et al. 2011; Narita et al. 2013; Mallonn et al. 2018) are also important to place further constraints on the spot covering fraction and thus to estimate, and correct for, the transit light source effect (e.g., Rosich et al. 2020). Such campaigns will be vital for all upcoming observations of smaller, temperature worlds, particularly for those around cooler stars (Apai et al. 2018). Long-term monitoring of LHS 1140 is especially crucial given the system also hosts a smaller (1.28 R_{\oplus}) but warmer (440 K) terrestrial planet (Feng et al. 2018; Ment et al. 2019) which, due to it is higher equilibrium temperature and lower surface gravity, could have larger spectral features and studies with future missions could allow comparative planetology within the same system.

6. Conclusions

Observing rocky, habitable-zone planets pushes the limits of our current technology. We have presented the HST WFC3 transmission spectrum of such a world and shown that it could be compatible with the presence of an atmosphere containing water. A popular aphorism suggests that the magnitude of a claim should be balanced by the weight of the evidence. Here, however, the evidence for water is marginal compared to a flat model, the primary or secondary nature of the atmosphere cannot be determined, and the signal could be distorted by stellar contamination. Hence more data is required to substantiate this claim and unveil the true nature of the planet, with future observatories possessing the power to do so.

This work is based upon observations with the NASA/ESA Hubble Space Telescope, obtained at the Space Telescope Science Institute (STScI) operated by AURA, Inc. The publicly available HST observations presented here were taken as part of proposal 14888, led by Jason Dittmann. These were obtained from the Hubble Archive which is part of the Mikulski Archive for Space Telescopes. This paper includes data collected by the TESS mission which is funded by the NASA Explorer

Program. TESS data is also publicly available via the Mikulski Archive for Space Telescopes.

This project has received funding from the European Research Council (ERC) under the European Union’s Horizon 2020 research and innovation program (grant agreement No. 758892, ExoAI) and under the European Union’s Seventh Framework Program (FP7/2007–2013)/ERC grant agreement numbers 617119 (ExoLights). Furthermore, we acknowledge funding by the Science and Technology Funding Council (STFC) grants: ST/K502406/1, ST/P000282/1, ST/P002153/1, and ST/S002634/1. Finally, this work was supported by Grant-in-Aid for JSPS Fellows, grant No. JP20J21872.

Software: Iraclis (Tsiaras et al. 2016b), TauREX3 (Al-Refaie et al. 2019), pylightcurve (Tsiaras et al. 2016a), ExoTETHyS (Morello et al. 1919), Astropy (Astropy Collaboration et al. 2018), h5py (Collette 2013), emcee (Foreman-Mackey et al. 2013), Matplotlib (Hunter 2007), Multinest (Feroz et al. 2009), Pandas (McKinney 2011), Numpy (Oliphant 2006), SciPy (Virtanen et al. 2020), corner (Foreman-Mackey 2016).

ORCID iDs

Billy Edwards  <https://orcid.org/0000-0002-5494-3237>
 Quentin Changeat  <https://orcid.org/0000-0001-6516-4493>
 Mayuko Mori  <https://orcid.org/0000-0003-1368-6593>
 Lara O. Anisman  <https://orcid.org/0000-0002-7771-6432>
 Mario Morvan  <https://orcid.org/0000-0001-8587-2112>
 Kai Hou Yip  <https://orcid.org/0000-0002-9616-1524>
 Angelos Tsiaras  <https://orcid.org/0000-0003-3840-1793>
 Ahmed Al-Refaie  <https://orcid.org/0000-0003-2241-5330>
 Ingo Waldmann  <https://orcid.org/0000-0002-4205-5267>
 Giovanna Tinetti  <https://orcid.org/0000-0001-6058-6654>

References

- Abel, M., Frommhold, L., Li, X., & Hunt, K. L. 2011, *JPCA*, 115, 6805
 Abel, M., Frommhold, L., Li, X., & Hunt, K. L. 2012, *JChPh*, 136, 044319
 Alexoudi, X., Mallonn, M., von Essen, C., et al. 2018, *A&A*, 620, A142
 Al-Refaie, A. F., Changeat, Q., Waldmann, I. P., & Tinetti, G. 2019, arXiv:1912.07759
 Apai, D., Rackham, B. V., Giampapa, M. S., et al. 2018, arXiv:1803.08708
 Astropy Collaboration, Price-Whelan, A. M., Sipőcz, B. M., et al. 2018, *AJ*, 156, 123
 Benneke, B., Wong, I., Piaulet, C., et al. 2019, *ApJL*, 887, L14
 Berta, Z. K., Charbonneau, D., Bean, J., et al. 2011, *ApJ*, 736, 12
 Changeat, Q., Edwards, B., Al-Refaie, A. F., et al. 2020, *AJ*, 160, 260
 Checlair, J., Menou, K., & Abbot, D. S. 2017, *ApJ*, 845, 132
 Claret, A. 2017, *A&A*, 600, A30
 Claret, A., Hauschildt, P. H., & Witte, S. 2012, *A&A*, 546, A14
 Claret, A., Hauschildt, P. H., & Witte, S. 2013, *A&A*, 552, A16
 Collette, A. 2013, Python and HDF5 (Sebastopol, CA: O’Reilly Media, Inc.)
 de Wit, J., Wakeford, H. R., Gillon, M., et al. 2016, *Natur*, 537, 69
 de Wit, J., Wakeford, H. R., Lewis, N. K., et al. 2018, *NatAs*, 2, 214
 Deming, D., Wilkins, A., McCullough, P., et al. 2013, *ApJ*, 774, 95
 Demory, B.-O., Gillon, M., Deming, D., et al. 2011, *A&A*, 533, A114
 Diamond-Lowe, H., Berta-Thompson, Z., Charbonneau, D., Dittmann, J., & Kempton, E. M. R. 2020, *AJ*, 160, 27
 Dittmann, J. A., Irwin, J. M., Charbonneau, D., et al. 2017, *Natur*, 544, 333
 Dressing, C. D., & Charbonneau, D. 2013, *ApJ*, 767, 95
 Dressing, C. D., Charbonneau, D., Dumusque, X., et al. 2015, *ApJ*, 800, 135
 Dressing, C. D., Newton, E. R., Schlieder, J. E., et al. 2017, *ApJ*, 836, 167
 Ducrot, E., Sestovic, M., Morris, B. M., et al. 2018, *AJ*, 156, 218
 Edwards, B., Changeat, Q., Hou Yip, K., et al. 2020, arXiv:2005.01684
 Edwards, B., Mugnai, L., Tinetti, G., Pascale, E., & Sarkar, S. 2019, *AJ*, 157, 242
 Edwards, B., Rice, M., Zingales, T., et al. 2019, *ExA*, 47, 29
 Feng, F., Tuomi, M., & Jones, H. R. A. 2018, arXiv:1807.02483
 Feroz, F., Hobson, M. P., & Bridges, M. 2009, *MNRAS*, 398, 1601
 Fletcher, L. N., Gustafsson, M., & Orton, G. S. 2018, *ApJS*, 235, 24

- Foreman-Mackey, D. 2016, *JOSS*, **1**, 24
- Foreman-Mackey, D., Hogg, D. W., Lang, D., & Goodman, J. 2013, *PASP*, **125**, 306
- Fulton, B. J., & Petigura, E. A. 2018, *AJ*, **156**, 264
- Fulton, B. J., Petigura, E. A., Howard, A. W., et al. 2017, *AJ*, **154**, 109
- Gettel, S., Charbonneau, D., Dressing, C. D., et al. 2016, *ApJ*, **816**, 95
- Gillon, M., Triaud, A. H. M. J., Demory, B.-O., et al. 2017, *Natur*, **542**, 456
- Gordon, I., Rothman, L. S., Wilzewski, J. S., et al. 2016, *DPS*, **48**, 421.13
- Herbst, K., Scherer, K., Ferreira, S. E. S., et al. 2020, *ApJL*, **897**, L27
- Howard, A. W., & Fulton, B. J. 2016, *PASP*, **128**, 114401
- Hunter, J. D. 2007, *CSE*, **9**, 90
- Ida, S., & Lin, D. N. C. 2008, *ApJ*, **673**, 487
- Ida, S., & Lin, D. N. C. 2010, *ApJ*, **719**, 810
- Ikoma, M., & Hori, Y. 2012, *ApJ*, **753**, 66
- Kane, S. R. 2018, *ApJL*, **861**, L21
- Kass, R. E., & Raftery, A. E. 1995, *Journal of the American Statistical Association*, **90**, 773
- Kreidberg, L., Bean, J. L., Désert, J.-M., et al. 2014, *Natur*, **505**, 69
- Lafreniere, D. 2017, NIRISS Exploration of the Atmospheric Diversity of Transiting Exoplanets (NEAT), JWST Proposal, Cycle 1, ID #1201
- Leitzinger, M., Odert, P., Kulikov, Y. N., et al. 2011, *P&SS*, **59**, 1472
- Li, G., Gordon, I. E., Rothman, L. S., et al. 2015, *ApJS*, **216**, 15
- Lillo-Box, J., Figueira, P., Leleu, A., et al. 2020, *A&A*, **642**, A121
- Lopez, E. D., Fortney, J. J., & Miller, N. 2012, *ApJ*, **761**, 59
- Mallonn, M., Herrero, E., Juvan, I. G., et al. 2018, *A&A*, **614**, A35
- McCullough, P., & MacKenty, J. 2012, Considerations for using Spatial Scans with WFC3, Instrument Science Report, *WFC3 2012-08*
- McKinney, W. 2011, pandas: a Foundational Python Library for Data Analysis and Statistics, Python, <https://pandas.pydata.org/docs/pandas.pdf>
- Ment, K., Dittmann, J. A., Astudillo-Defru, N., et al. 2019, *AJ*, **157**, 32
- Mordasini, C., Alibert, Y., & Benz, W. 2009, *A&A*, **501**, 1139
- Morello, G., Claret, A., Martin-Lagarde, M., et al. 1919, *AJ*, **159**, 75
- Narita, N., Fukui, A., Ikoma, M., et al. 2013, *ApJ*, **773**, 144
- Nettelmann, N., Fortney, J. J., Kramm, U., & Redmer, R. 2011, *ApJ*, **733**, 2
- Ogihara, M., Morbidelli, A., & Guillot, T. 2015, *A&A*, **578**, A36
- Oliphant, T. E. 2006, A guide to NumPy, Vol. 1 (Spanish Fork, UT: Trelgol)
- Owen, J. E., & Jackson, A. P. 2012, *MNRAS*, **425**, 2931
- Owen, J. E., & Wu, Y. 2013, *ApJ*, **775**, 105
- Owen, J. E., & Wu, Y. 2017, *ApJ*, **847**, 29
- Pluriel, W., Whiteford, N., Edwards, B., et al. 2020, *AJ*, **160**, 112
- Polyansky, O. L., Kyuberis, A. A., Zobov, N. F., et al. 2018, *MNRAS*, **480**, 2597
- Rackham, B. V., Apai, D., & Giampapa, M. S. 2018, *ApJ*, **853**, 122
- Ricker, G. R., Winn, J. N., Vanderspek, R., et al. 2014, *Proc. SPIE*, **9143**, 914320
- Rogers, L. A., & Seager, S. 2010, *ApJ*, **716**, 1208
- Rosich, A., Herrero, E., Mallonn, M., et al. 2020, *A&A*, **641**, A82
- Rothman, L. S., Gordon, I. E., Barber, R. J., et al. 2010, *JQSRT*, **111**, 2139
- Skaf, N., Bieger, M. F., Edwards, B., et al. 2020, *AJ*, **160**, 109
- Smith, J. C., Stumpe, M. C., van Cleve, J. E., et al. 2012, *PASP*, **124**, 1000
- Spinelli, R., Borsa, F., Ghirlanda, G., et al. 2019, *A&A*, **627**, A144
- Stevenson, K. B., & Fowler, J. 2019, arXiv:1910.02073
- Stumpe, M. C., Smith, J. C., Catanzarite, J. H., et al. 2014, *PASP*, **126**, 100
- Stumpe, M. C., Smith, J. C., van Cleve, J. E., et al. 2012, *PASP*, **124**, 985
- Tennyson, J., Yurchenko, S. N., Al-Refaie, A. F., et al. 2016, *JMoSp*, **327**, 73
- Tinetti, G., Drossart, P., Eccleston, P., et al. 2018, *ExA*, **46**, 135
- Smith, J. C., Stumpe, M. C., van Cleve, J. E., et al. 2012, *PASP*, **124**, 1000
- Tsiaras, A., Waldmann, I., Rocchetto, M., et al. 2016a, pylightcurve: Exoplanet lightcurve model, Astrophysics Source Code Library, ascl:1612.018
- Tsiaras, A., Waldmann, I. P., Rocchetto, M., et al. 2016b, *ApJ*, **832**, 202
- Tsiaras, A., Waldmann, I. P., Tinetti, G., Tennyson, J., & Yurchenko, S. N. 2019, *NatAs*, **3**, 1086
- Tsiaras, A., Waldmann, I. P., Zingales, T., et al. 2018, *AJ*, **155**, 156
- Valencia, D., Guillot, T., Parmentier, V., & Freedman, R. S. 2013, *ApJ*, **775**, 10
- Virtanen, P., Gommers, R., Oliphant, T. E., et al. 2020, *NatMe*, **17**, 261
- Wakeford, H. R., Lewis, N. K., Fowler, J., et al. 2019, *AJ*, **157**, 11
- Wunderlich, F., Godolt, M., Grenfell, J. L., et al. 2019, *A&A*, **624**, A49
- Yang, J., Ji, W., & Zeng, Y. 2020, *NatAs*, **4**, 58
- Yip, K. H., Changeat, Q., Edwards, B., et al. 2020a, arXiv:2009.10438
- Yip, K. H., Tsiaras, A., Waldmann, I. P., & Tinetti, G. 2020b, *AJ*, **160**, 171
- Yurchenko, S. N., Barber, R. J., & Tennyson, J. 2011, *MNRAS*, **413**, 1828
- Yurchenko, S. N., & Tennyson, J. 2014, *MNRAS*, **440**, 1649
- Zeng, L., Jacobsen, S. B., Sasselov, D. D., et al. 2019, *PNAS*, **116**, 9723
- Zhang, Z., Zhou, Y., Rackham, B. V., & Apai, D. 2018, *AJ*, **156**, 178